In the format provided by the authors and unedited.

Energy-dependent path of dissipation in nanomechanical resonators

J. Güttinger, A. Noury, P. Weber, A.M. Eriksson, C. Lagoin, J. Moser,
C. Eichler, A. Wallraff, A. Isacsson, A. Bachtold

S.1   Device Parameters

Important parameters of the measured devices are summarized in Table S1 and described in more details in the following sections.

S.2   Device layout

The device layout is optimized to maximize the readout sensitivity, minimize parasitic heating and ensure compatibility with the JPA readout (Fig. S1). The device consists of a suspended graphene drum which couples capacitively to the cavity over a circular counter-electrode (red in Figs. S1a,b). Devices are fabricated by first structuring a Nb film with reactive ion etching, and then transferring a graphene flake onto the Nb structure. A detailed description of the fabrication can be found in Ref. [1]. We use a quarter-wavelength microwave cavity (Fig. S1c). In order to reduce internal losses of the cavity over the graphene electrodes, we fabricate capacitors with $C_{\mathrm{LP}} \approx 1 - 2\,\mathrm{pF}$ to the ground plane of the chip at the end of the electrodes. To reduce the heat dissipation of the graphene device we evaporate $3/40\,\mathrm{nm}$ of Cr/Au onto the Nb lines in device I (yellow in Fig. S1). For a JPA compatible readout, the cavity is capacitively connected to both a weakly coupled port and a strongly coupled port. This layout prevents the saturation of the amplifier by the strong pump tone at ω_{p} in a transmission measurement configuration. That is, the pump signal is attenuated by the cavity by $\approx 40\,\mathrm{dB}$. The output signal of the cavity is not deteriorated by the weakly coupled port, since the decay of the cavity through this port is small compared to that of the strongly coupled port. The separation between the weak port (green in Fig. S1c) and the strong port (blue) is large in order to reduce residual coupling between the input and output ports.

Table S1: **Device parameters.** The dimensions of the mechanical resonators are measured with an atomic force microscope. The initial separation of the graphene drum and the gate electrode is estimated from the height difference between the graphene contact electrodes and the gate electrode. The resonance frequency of the lowest mechanical mode is $\omega_1/2\pi$. The effective mass m_{eff} of the few layer graphene drums is given in terms of the effective mass of a single layer graphene drum $m_{\text{eff},0} \approx 1.6$ fg. The cavity is characterized by its resonance frequency ω_{c} and its total coupling rate κ_{tot}, which is composed of the external coupling rate κ_{ext} and the internal loss rate κ_{int}. The voltage in brackets is the DC electrode voltage V_{g} at which the parameter is measured. The single-photon optomechanical coupling g_0 is calibrated from thermal motion measurements in device I and III. For device II the coupling is calibrated from the driven motion as described in Ref. [1].

|	Device I	Device II	Device III	Section
Graphene device				
Drum radius	1.65 μm	1.6 μm	1.6 μm	S.2
Cavity electrode radius	1.1 μm	1.1 μm	1.2 μm	
Graphene cavity-electrode separation	85 nm	90 nm	88 nm	
Graphene contacts	Nb and Au	Nb	Nb	S.2
$\omega_1/2\pi$	46 MHz (0.6 V)	44 MHz (-3.3 V)	67 MHz (0 V)	
Effective mass	$6 \times m_{\text{eff},0}$	$35 \times m_{\text{eff},0}$	$25 \times m_{\text{eff},0}$	S.4.1
Cavity				S.3.1
$\omega_{\text{c}}/2\pi$ (0 V)	7.48788 GHz	7.43778 GHz	7.4244 GHz	
$\kappa_{\text{tot}}/2\pi$ (0 V)	2.5 MHz	3.2508 MHz	1.8 MHz	
$\kappa_{\text{ext}}/2\pi$ (0 V)	1.7 MHz	1.3176 MHz	850 kHz	
$\kappa_{\text{int}}/2\pi$ (0 V)	800 kHz	1.9324 MHz	950 kHz	
Coupling				
$g_0/2\pi$	7.3 Hz (0 V)	2.95 Hz (-3.3 V)	9.7 Hz (0 V)	S.5
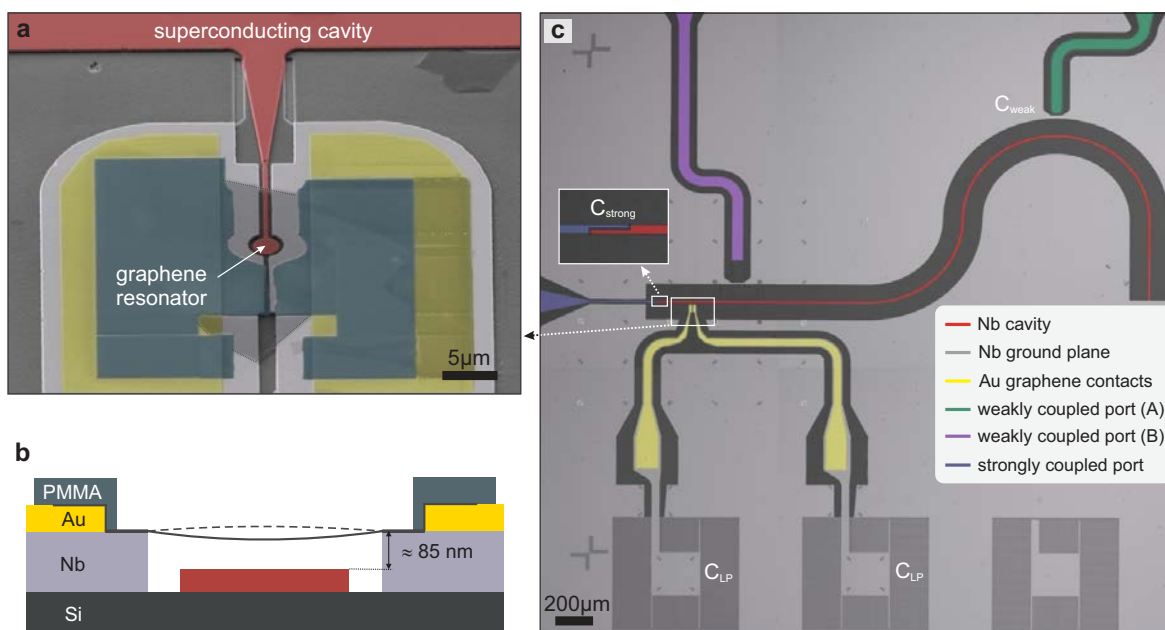
Figure S1: **Coupled graphene-superconducting cavity device. a**, Colored scanning electron microscopy image of device I. The graphene resonator is coupled to a superconducting niobium cavity (red). The circular graphene drum is suspended over the circular cavity counter-electrode and clamped on the sides between gold electrodes (yellow) and crosslinked Polymethylmethacrylate (PMMA, dark green). The graphene flake is clamped on the two sides of its surface in order to improve the attachment to the support. **b**, Cross-section of the graphene drum. **c**, Superconducting cavity with coupling ports and graphene contact electrodes. On-chip capacitors $C_{\mathrm{LP}} \approx 1-2$ pF between the graphene contact electrodes and the ground reduce the internal loss of the cavity. In a reflection measurement, the cavity is probed using the strongly coupled port. In a transmission measurement, the weakly coupled port is used as the input (C_{weak}) and the strongly coupled port as the output (C_{strong}). In device II the purple line is used as weak port.

S.3   Measurement setup

Figure S2 shows a detailed schematic of the measurement setup. We carry out the measurements with a Triton 200 dilution refrigerator from Oxford instruments with a base temperature of 15 mK. The RF-lines are UT85-SS-SS coaxial cables from room temperature to the 700 mK stage and superconducting UT85-Nb-Nb coaxial cables at lower temperatures. For the cavity and JPA pump tones we use two Agilent E8257D PSG microwave sources. An Agilent N5181A microwave source is used for the low frequency drive. As for the directional couplers, we use a 10 dB Pasternack PE2204 on the transmission port, a 20 dB Arra 5191-20 on the reflection port and a 20 dB Krytar 120420 in front of the JPA. The circulators are CTH0408KC from Quinstar. The DC voltage source used to apply V_{g} is a SIM928 from Standford Research Systems. The DC line is filtered with π-filters at room temperature and a home made RC filter at the mixing chamber. A Bias Tee ZFBT-6GW from minicircuits connects the DC line and the low frequency drive line.

We use a digitally variable attenuator TEA13000-12 and a variable phase shifter TEP8000-6 from Telemakus to attenuate the pump tone by ≈ 40 dB. We do not need to cancel the JPA pump tone as the double cavity design [2] allows to pump the JPA with a detuning of ≈ 200 MHz from the signal. An additional SIM928 DC voltage source is used to generate a current through a flux coil underneath the JPA and thereby tune the frequency of the JPA amplification band (not shown). The cryogenic HEMT is an LNF-LNC4_8A from Low Noise Factory. For spectral measurements we use an Agilent MXA N9020A with integrated preamplifier.

A detailed schematic of the energy decay measurement setup is shown in Fig. S3. To stop the mechanical drive signal and initiate the energy decay, we use a ZASW-2-50DR+ RF switch from Mini-Circuits. The switch is triggered with a square-wave signal generated with a NI PXI 5451 AWG from National Instruments. Because of the optomechanical coupling, the mechanical response is frequency up-converted to the cavity resonance frequency ω_{c}. At the output of the cryostat, the signal at the pump frequency is attenuated with a tunable bandpass-filter WBCQV 7000/8000-6SSSD from Wainwright Instruments. This is to avoid saturation during amplification of the signal with the subsequent low-noise amplifiers AMF-4F-04000800-07-10P and AMF-3F-04000800-07-10P from MITEQ. To damp reflections from the amplifiers, isolators D3I6012 from Ditom are used in front of the amplifiers. The signal is down-mixed using an I-Q mixer IQ-4509LXP from Marki Microwave to the intermediate frequency $\omega_{\mathrm{IF}} = 500$ kHz. The mixing tone is generated by a ZVB-14 from Rhode and Schwarz. The I and Q quadratures are independently filtered with a 1.9 MHz lowpass filter BLP 1.9+ from Mini-Circuits and amplified by a SR-560 preamplifier from Stanford Research. The preamplifier has an additional high pass filter at 10 kHz and a low pass filter at 1 MHz. We record the two quadratures using a two channel digitizer NI PXI 5114 from National Instruments. The digitizer and the trigger generator are synchronized with the internal PXI bus.
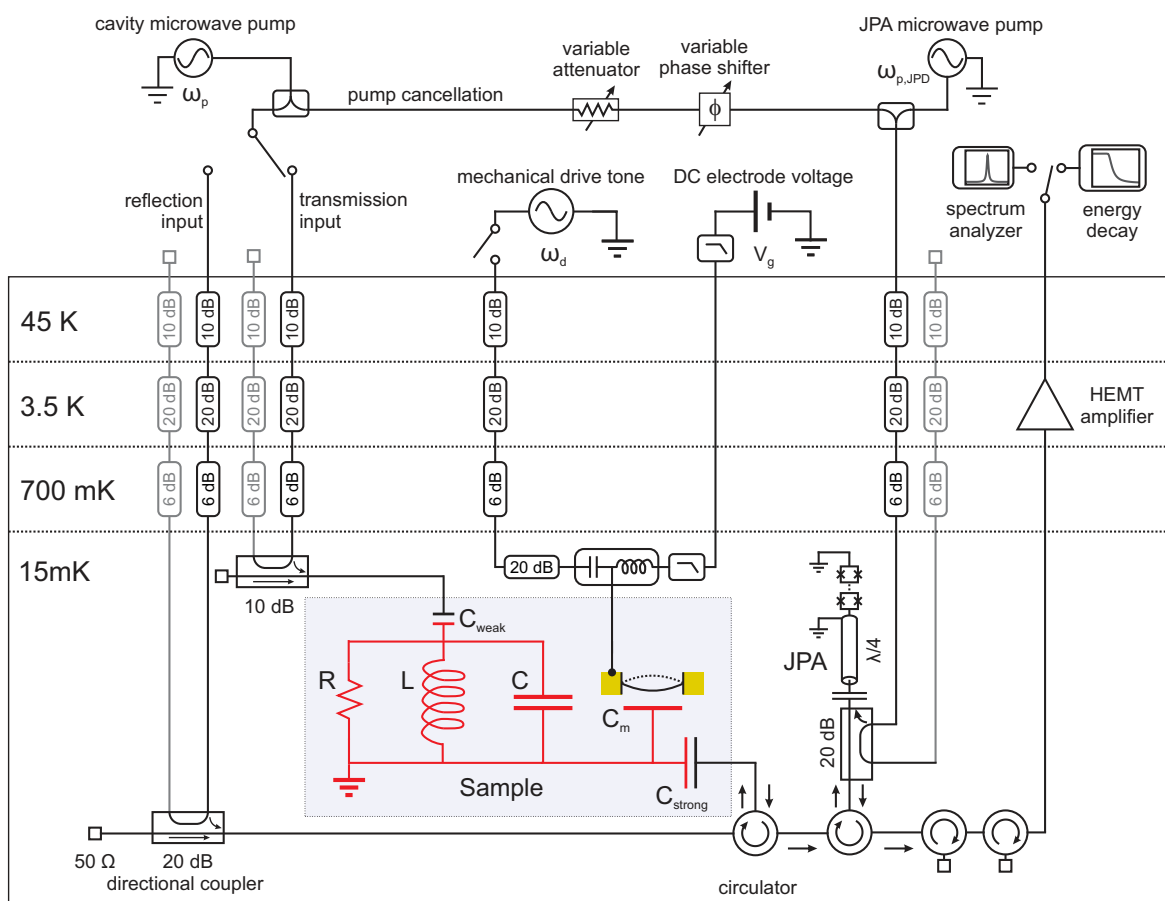
Figure S2: **Measurement setup with cryogenic wiring.** The detailed schematic shows the cancellation of the cavity pump tone, the wiring of the Josephson parametric amplifier (JPA) and the filtering of the lines. In addition to reflection measurements over the strongly coupled cavity port (C_{strong}), we measure the cavity in transmission by coupling the pump signal using a weakly coupled port (C_{weak}). The asymmetric coupling allows to attenuate the residual cavity pump tone at the output of the cavity, without creating a significant additional loss channel for the signal. To avoid saturation of the JPA, the pump tone is further attenuated by a cancellation tone in front of the JPA. The JPA is operated as a non-degenerate reflection amplifier. All radio frequency input lines are attenuated at different temperature stages to eliminate thermal noise. At the 15 mK stage, directional couplers are used instead of attenuators to minimize the heat load. The thermal noise entering the output line is attenuated with circulators.
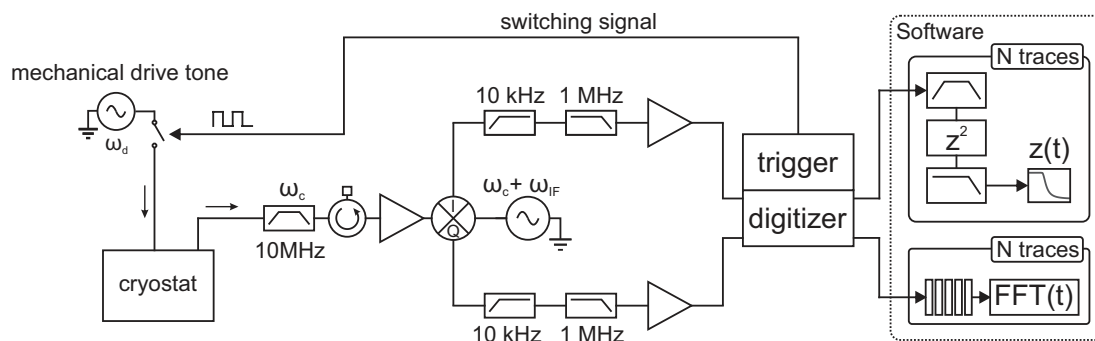
Figure S3: **Detailed energy decay measurement setup.**

To record energy decay measurements we pump the cavity with an electromagnetic field with frequency $\omega_p = \omega_c - \omega_d$. Here, $\omega_c \approx 7.5$ GHz is the cavity resonance frequency and ω_d is the mechanical drive frequency with $\omega_d \approx \omega_1$. The optomechanical coupling leads to an anti-Stokes scattered field around frequency ω_c. The signal is then down-mixed from ω_c to 500 kHz using an I/Q frequency mixer. The down-mixed signal is then digitized, digitally band-pass filtered around 500 kHz with bandwidth BW, squared and eventually low pass filtered with bandwidth $BW/2$. We set $BW \approx 2$ kHz for measurements with low vibrational amplitudes (Fig. 2 of the main text), and $BW = 150 - 400$ kHz for measurements with large vibrational amplitudes in order to account for changes in the vibrational frequency of the mechanical resonator (Fig. 3 of the main text). In order to subtract the amplifier noise contribution from the mechanical signal, we compute the time-averaged signal at the end of each decay traces (when the vibration amplitude is suppressed to zero). This noise subtraction has been applied for all amplitude ring-down measurements presented throughout the paper.

S.3.1   Characterization of superconducting cavity

In Fig. S4 we plot the reflected $|S_{11}|^2$ and transmitted $|S_{12}|^2$ power as well as the phase shift of the reflected signal at $T = 15$ mK. To extract the internal loss rate κ_{int} and the decay rate thought the external ports $\kappa_{\text{ext}} = \kappa_{\text{weak}} + \kappa_{\text{strong}}$ we make use of the fact that the external loss over the weak port is negligible $\kappa_{\text{weak}} < 2\pi \cdot 60$ kHz $<< \kappa_{\text{strong}}$. In the reflection measurement using the strong port with $\kappa_{\text{ext}} \approx \kappa_{\text{strong}}$, the line shape is described by [3]

$$S_{11} = \frac{\kappa_{\text{int}} - \kappa_{\text{ext}} - 2i(\omega - \omega_c)}{\kappa_{\text{int}} + \kappa_{\text{ext}} - 2i(\omega - \omega_c)}. \tag{S1}$$

A fit of the reflected signal to this equation yields $\kappa_{\text{ext}}/2\pi = 1.7$ MHz and $\kappa_{\text{int}}/2\pi = 0.8$ MHz.
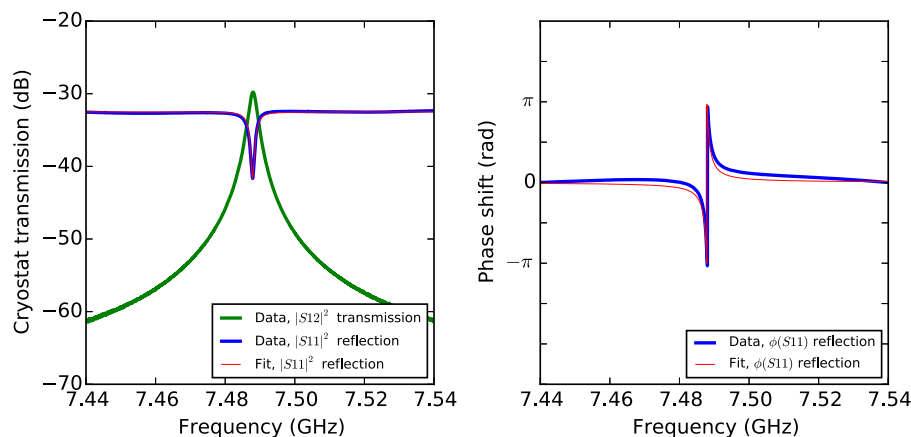
Figure S4: **Transmission and reflection measurement of the superconducting cavity in device I.** The measurements include the cryostat wiring and the cryogenic HEMT amplifier. The strongly coupled port is denoted with 1 and the weakly coupled port with 2.

S.3.2   Noise reduction with the Josephson parametric amplifier (JPA)

The JPA significantly improves the detection efficiency of energy decay measurements, as illustrated in Fig. S5. The red trace is recorded with the JPA turned on, while the blue trace corresponds to the measurements with the JPA switched off. For the chosen gain of 26 dB we observe a noise rise of 15 dB in spectral measurements when turning on the JPA. As a result, the effective system noise is dominated by the noise of the JPA with only a small contribution from the HEMT noise and cable losses after the JPA. The JPA used in our setup has been demonstrated to operate close to the quantum limit [2].

S.4   Tuning of the mechanical resonance frequencies with gate voltage

S.4.1   Effective mass of the fundamental mode of the mechanical resonator

In order to determine the mass of the three devices, we apply different methods. For device I we measure the mechanical resonance frequency as a function of gate voltage, see Fig. S6, and we check that the obtained mass is consistent with the graphene thickness estimated from optical contrast measurements. At large gate voltage, the resonant fre-
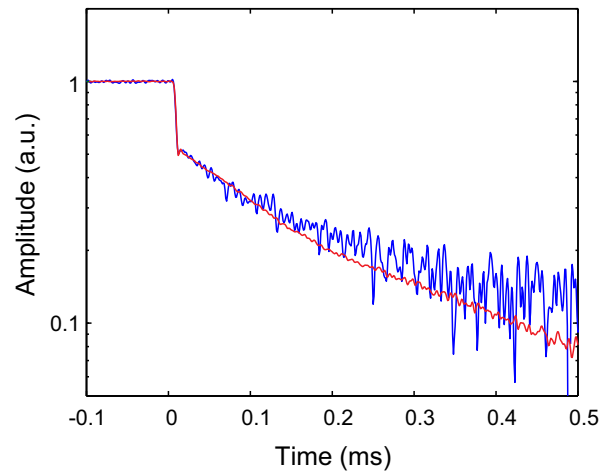
Figure S5: **Improvement of measurement quality with the Josephson parametric amplifier (JPA).** The figure shows the decay trace with the JPA turned on (red) and the measurement with the JPA pump switched off (blue).
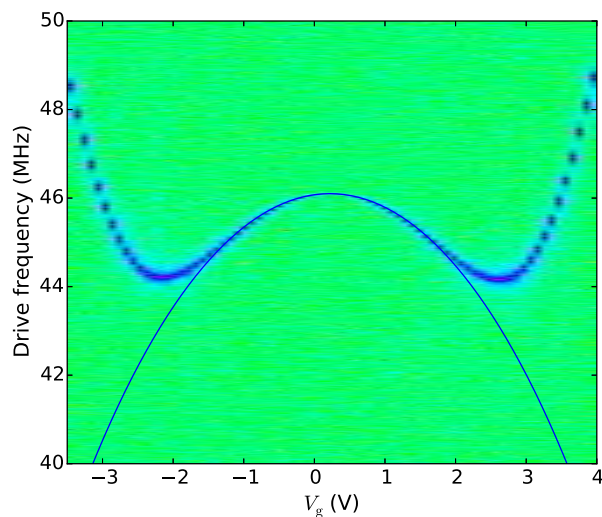

Figure S6: **Mechanical resonance frequency as a function of Vg.** The blue line corresponds to a fit of the measurement to Eq. (S2) for low $|V_g|$.

quency becomes higher when increasing $|V_g|$, because of the variation of the mechanical tension in the graphene flake. Near $V_g = 0\,\text{V}$, we observe the opposite behaviour, which is attributed to capacitive softening. We quantify the effective mass m_{eff} of the resonator by comparing these measurements to the predictions of capacitive softening for a circular drum under tensile tension separated from the gate electrode by the distance d [1],

$$\omega_1(V_g) = \sqrt{\omega_1(0) - \frac{0.271}{m_{\text{eff}}}\frac{\epsilon_0 \pi R_g^2}{d^3}V_g^2}. \tag{S2}$$

Here R_g is the radius of the gate electrode, and $\omega_1(0)$ the frequency at $V_g = 0\,\text{V}$. The effective mass $m_{\text{eff}} = 0.27\pi R \rho_{\text{2D}}$ is further decomposed into the radius R of the circular resonator and the two-dimensional mass density $\rho_{\text{2D}} = n_g \rho_{\text{graphene}}$ with n_g the number of graphene layers and $\rho_{\text{graphene}} = 7.6 \times 10^{-19}\,\text{kg}/\mu\text{m}^2$. Prior to cooling down the device, we use atomic force microscopy to determine the geometrical device parameters to be $R = 1.65\,\mu\text{m}$, $R_g = 1.1\,\mu\text{m}$, and $d = 85\,\text{nm}$. The fit shown in Fig. S6 is obtained using a mass that corresponds to $n_g = 5.5$ graphene layers and a voltage offset $V_{\text{offset}} = 0.25\,\text{V}$ which is attributed to the work function difference between the graphene membrane and the cavity electrode. Probing the number of graphene layers by means of optical contrast measurements [5, 6] yields $n_g \approx 6$, which is in good agreement with the value obtained with the other method. For the device II, we measure the thickness of the graphene flake by atomic force microscopy (AFM) and divide the obtained value by $0.335\,\text{nm}$, the thickness of a single graphene layer [5]. We measure a thickness of $t = 12\,\text{nm}$ and estimate ≈ 35 equivalent graphene layers. For device III we estimate ≈ 25 graphene layers, obtained as an average from AFM measurements and a fit to the gate dependence of the mechanical resonance frequency.

S.4.2 Gate voltage dependence of the resonant frequencies of the mechanical modes of device II

Figure S7 shows the detectable resonant frequencies of the mechanical modes of device II as a function of the DC voltage V_g applied between the graphene flake and the cavity. The resonant frequencies are extracted from driven spectra recorded with a high driving force amplitude and a high pump power ($V_d = 120\,\mu\text{V}$, $P_{\text{pump}} = 13\,\text{mW}$ at the input of the cryostat). The lines in the figure are parabolic guides to the eye. Since the V_g dependencies of the resonant frequency are different for the different modes, it is possible to set the frequency ratio of two modes to an integer by applying the appropriate V_g values.
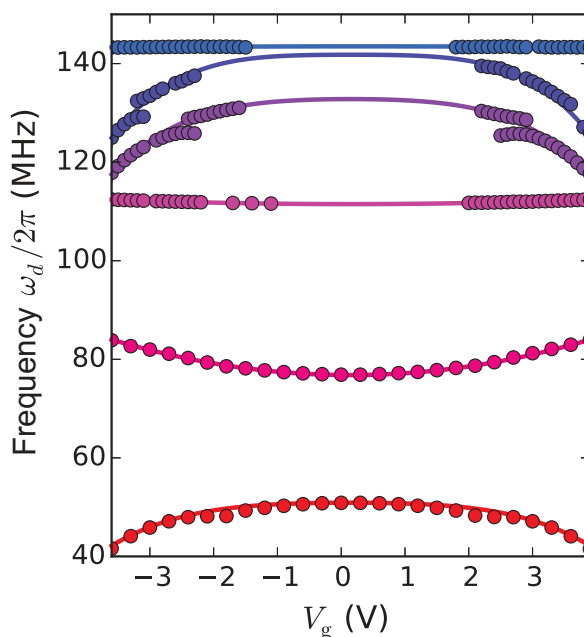
Figure S7: **Mode spectrum of device II.** Fundamental and higher mechanical mode spectrum are extracted from driven measurements.

S.5 Thermal motion and calibration of vibrational amplitude

The integrated area of the thermal resonance is a direct probe of the temperature of the mechanical mode and therefore allows for the calibration of the mechanical phonon occupation (Fig. S8). The area is linearly proportional to the motional variance $\langle z^2 \rangle$ and thus directly linked to the temperature of the mode T_{m} through the equipartition theorem $1/2 m_{\mathrm{eff}} \omega_{\mathrm{m}}^2 \langle z^2 \rangle = 1/2 k_{\mathrm{B}} T_{\mathrm{m}}$. Here, ω_{m} is the resonant angular frequency of the graphene resonator. In Fig. S8b we plot the peak area of device I as a function of the cryostat temperature T_{cryo}. Above $T_{\mathrm{cryo}} = 60$ mK, the area is proportional to the cryostat temperature in agreement with the equipartition theorem such that we assign $T_{\mathrm{m}} = T_{\mathrm{cryo}}$ and extract the resonator phonon occupation $n_{\mathrm{m}} = \frac{k_{\mathrm{B}} T_{\mathrm{m}}}{\hbar \omega_{\mathrm{m}}}$. From this calibration, we obtain an occupation of 20 phonons for the spectrum in Fig. S8a and an average of $n_{\mathrm{m}} = 25 \pm 5$ over many spectra at base temperature. The saturation of the mode temperature below $T_{\mathrm{bath}} = 60$ mK is attributed to the heating induced by the pump field (see below).

Based on this measurement, we are also able to accurately calibrate the single-photon optomechanical coupling g_0 of the mechanical resonator to the cavity [4]. It is inferred from the area of the thermal resonance measured as the output power $P_{\mathrm{out}} = \int S_{\mathrm{N}} d\omega / 2\pi$ at the level of the spectrum analyzer and the input power P_{in} applied at the input port of the cryostat. Here, S_{N} is the single sided power spectral density. The ratio $P_{\mathrm{out}}/P_{\mathrm{in}}$ reads
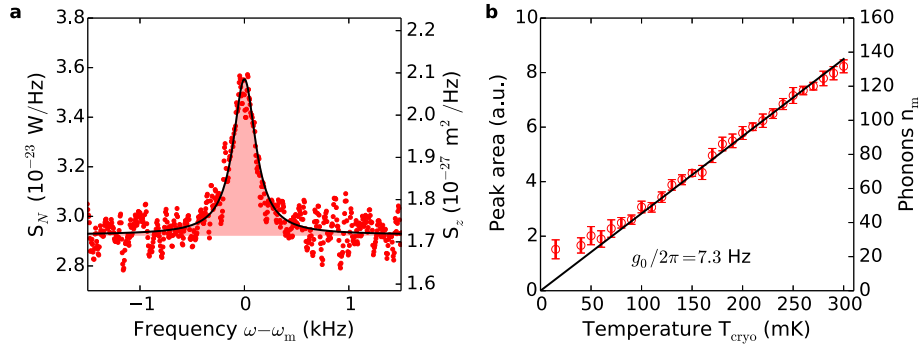
Figure S8: **Thermal calibration of device I.** Power spectral density (S_{N}) and displacement spectral density (S_{z}) of the thermal motion measured at base temperature $T_{\mathrm{cryo}} = 15\,\mathrm{mK}$ with a photon number $n_{\mathrm{p}} = 1.9 \cdot 10^5$. **b**, Calibration of the area of the thermal peak as a function of cryostat temperature at a photon number $n_{\mathrm{p}} = 1.9 \cdot 10^5$ for $T_{\mathrm{bath}} < 150$ mK and $n_{\mathrm{p}} = 3.8 \cdot 10^5$ for $T_{\mathrm{bath}} > 150$ mK. The linear slope at high temperature allows us to convert the peak area into the phonon number. The slope yields the opto-mechanical coupling strength $g_0/2\pi = 7.3$ Hz. The minimum mechanical phonon occupation is $n_{\mathrm{m}} = 25$ at the base temperature of the cryostat, which is 15 mK.

$$\frac{P_{\mathrm{out}}(\omega_{\mathrm{c}})}{P_{\mathrm{in}}(\omega_{\mathrm{p}})} = 4g_0^2 \cdot gain \cdot loss \cdot \frac{\kappa_{\mathrm{ext}}^2}{\kappa_{\mathrm{tot}}^2} \frac{1}{\omega_{\mathrm{m}}^2} \frac{k_{\mathrm{B}}}{\hbar\omega_{\mathrm{m}}} T_{\mathrm{m}}, \tag{S3}$$

with the total cavity decay rate $\kappa_{\mathrm{tot}} = \kappa_{\mathrm{int}} + \kappa_{\mathrm{ext}}$. We determine the product $loss \cdot gain = -30.25\,\mathrm{dB}$ by measuring the transmitted power through the cryostat at ω_{c} (green curve in Fig. S4). From the data in Fig. S8b, we obtain $g_0 = 2\pi \times 7.3\,\mathrm{Hz}$. For this calibration to be precise, we verify that the response of the transmitted power through our input and output lines remains constant over the frequency range between ω_{c} and ω_{p}. In energy decay measurements, we use this calibration in order to convert measured power into vibration amplitude.

S.6 Energy decay in the low vibrational amplitude regime

S.6.1 Comparison between γ_{decay} and $\gamma_{\mathrm{spectral}}$

We compare the energy decay rate γ_{decay} obtained from ring down measurements with the line-width $\gamma_{\mathrm{spectral}}$ of the thermal resonance of spectral measurements (Fig. S9). Thermal spectra are fitted with a Lorentzian (red lines) to extract $\gamma_{\mathrm{spectral}}$. For comparison, the black dotted lines correspond to Lorentzian resonances with the width γ_{decay} that is
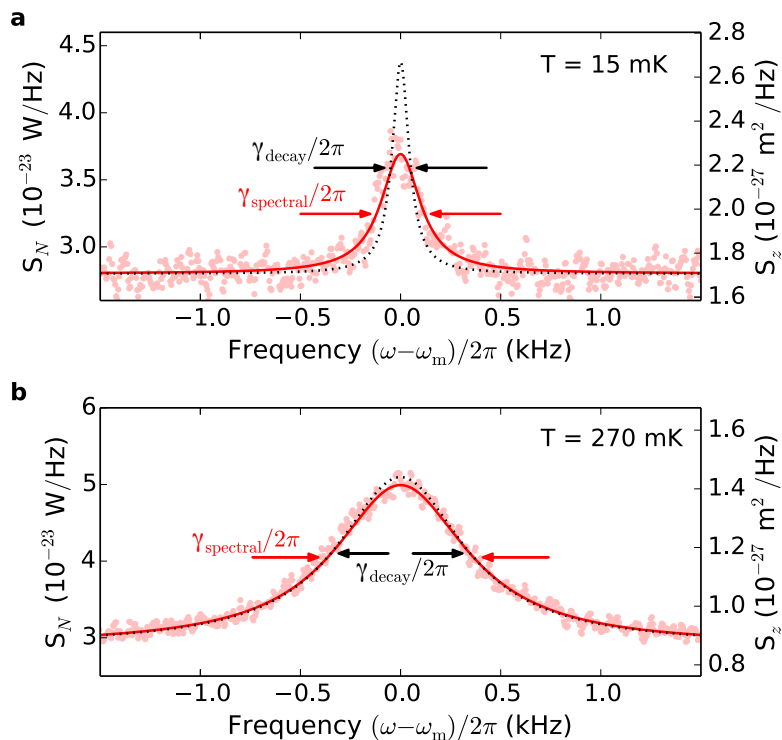
Figure S9: **Comparison of spectral line-width and energy decay rate in device I. a**, Power spectral density at the output of the cavity (S_N) and displacement spectral density (S_z) of a typical thermal motion spectrum measured at $T_{cryo} = 15\,\mathrm{mK}$ (red data point), yielding $\gamma_{spectral}/2\pi = 300$ Hz. Using the same n_p and V_g, we obtain $\gamma_{decay}/2\pi = 130$ Hz from energy decay measurements. The corresponding spectrum is plotted as a black dotted Lorentzian. We set $n_p = 1.9 \cdot 10^5$ and $V_g = 0$ V. **b**, Thermal spectrum at $T_{cryo} = 270$ mK, yielding $\gamma_{spectral}/2\pi = 800$ Hz . We get $\gamma_{decay}/2\pi = 760$ Hz from energy decay measurements. These measurements are recorded with $n_p = 3.8 \cdot 10^5$ and $V_g = 0$ V.
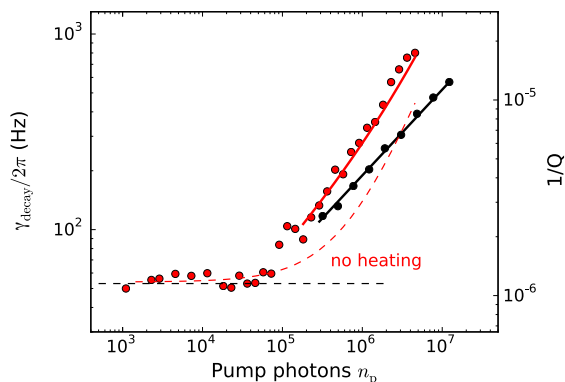
Figure S10: **Dependence of the energy decay rate on cavity pump photons.**
Energy decay rate while pumping the cavity either on the red sideband (red points) or on
cavity resonance (black points) in device I. The dashed red line corresponds to $\gamma_{\text{decay}} = \gamma_{\text{m0}} + \Gamma_{\text{opt}}$ where γ_{m0} is the intrinsic decay rate obtained at low n_{p} and $\Gamma_{\text{opt}} = 4n_{\text{p}}g_0^2/\kappa$
the optomechanical damping. The continuous red line is obtained by including the effect
of Joule heating, that is, by taking into account the n_{p} dependence of γ_{m0} (black line).

obtained from energy decay measurements. Figure S9a shows resonances at the cryostat
base temperature, which is $T_{\text{cryo}} = 15$ mK. The spectral linewidth $\gamma_{\text{spectral}} \approx 2\pi \times 300$ Hz
is more than twice as large as $\gamma_{\text{decay}} \approx 2\pi \times 130$ Hz. Dephasing accounts for about 50% of
the spectral linewidth. Spectral measurements and energy decay measurements are both
obtained with $n_{\text{p}} = 1.9 \cdot 10^5$ and $V_{\text{g}} = 0$ V. This value of n_{p} leads to heating as we will
discuss below in section S.6.2.

The difference between γ_{spectral} and γ_{decay} is greatly reduced at higher temperature.
For instance, the difference is suppressed to 40 Hz at 270 mK (Fig. S9b). Dephasing
accounts for about 5% of the spectral linewidth.

S.6.2 Dependence of energy decay rate on pump field amplitude

We plot γ_{decay} as a function of the number n_{p} of pump photons in the cavity for device I
at the cryostat temperature $T_{\text{cryo}} = 15$ mK (red data points in Fig. S10). For $n_{\text{p}} < 10^5$,
we observe that the decay rate remains constant $\gamma_{\text{m0}} \approx 50$ Hz over a large range of n_{p}.
Upon increasing n_{p} above 10^5, γ_{decay} gets larger. We show below that the increase of
γ_{decay} is due both to optomechanical damping and to Joule heating induced by the pump
electromagnetic field.

These data are recorded by pumping the cavity on the red detuned sideband $\omega_p = \omega_c - \omega_m$. The resulting optomechanical damping $\Gamma_{\text{opt}} = 4n_{\text{p}}g_0^2/\kappa$, shown with the red dashed
line in Fig. S10, is lower than the measured γ_{decay}. This indicates that optomechanical
damping alone cannot account for our data.

We quantify the effect of Joule heating by pumping the cavity at $\omega_{\mathrm{p}} = \omega_{\mathrm{c}}$ and recording energy decay traces at both $\omega_{\mathrm{c}} - \omega_{\mathrm{p}}$ and $\omega_{\mathrm{c}} + \omega_{\mathrm{p}}$. Pumping at $\omega_{\mathrm{p}} = \omega_{\mathrm{c}}$ leads to $\Gamma_{\mathrm{opt}} = 0$ Hz. We observe that γ_{decay} gets larger upon increasing n_{p} (black data points in Fig. S10). This increase of γ_{decay} is attributed to Joule heating. This measurement can be described by $\gamma_{\mathrm{decay}} \propto n_{\mathrm{p}}^{0.43}$ (black line in Fig. S10).

By adding this n_{p} dependence of γ_{decay} due to Joule heating together with $\Gamma_{\mathrm{opt}} = 4 n_{\mathrm{p}} g_0^2 / \kappa$, we quantitatively reproduce the measurement of γ_{decay} as a function of n_{p} (red line in Fig. S10).

S.7 Energy decay in the high vibrational amplitude regime

S.7.1 Measurement of the instantaneous vibrational frequency during the decay

The vibration frequency during the decay is obtained with short-time Fourier transform (STFT). This method is suitable for the analysis of signals with time-varying frequency spectrum. We use a Hamming apodization function to segment the signal in temporal windows. Such a process allows us to reduce spectral components that are due to the temporal window itself, while keeping a good frequency resolution of the analyzed signal. For a time varying signal $z(t)$, its STFT is expressed as

$$Z(t, \omega) = \int_{-\infty}^{+\infty} z(t') \cdot \mathrm{Ham}(t - t') \cdot e^{-j \cdot \omega \cdot t'} dt'. \tag{S4}$$

We use a Hamming apodization function $\mathrm{Ham}(t)$ with a window width of 200 μs. The STFT is calculated with a frequency resolution of 610 Hz. The plotted STFT at time t is the average of the STFT of 1000 individual energy decay traces (Fig. S11a).

In addition to the smooth decay of the eigenfrequency described in the main text, we observe a jump in frequency from ω_{d} to $\omega_{\mathrm{m,max}}$ in Fig. S11a. The jump is faster than the time resolution of the Fourier transformation. Furthermore, the jump is consistent with the dynamics of a resonator when it undergoes the transition between the driven and the non-driven regime (see schematic in Fig. S11b). In the driven regime, the resonator is forced to oscillate at ω_{d}, whereas the eigenfrequency $\omega_{\mathrm{m}}(z)$ of a resonator in the non-driven regime only depends on the vibrational amplitude, as indicated by the red line in Fig. S11b. The jump from ω_{d} to $\omega_{\mathrm{m,max}}$ is expected to be quasi-instantaneous, as the motion during the free decay has no frequency memory and depends only on the initial displacement and velocity at $t = 0$. Since the total energy of the resonator $E_{\mathrm{m}} = 1/2 m_{\mathrm{eff}} \omega(t)^2 z(t)^2$ remains constant over $t \ll 1/\gamma_{\mathrm{decay}}$, the observed jump in ω should in principle be associated with a change in z. For the observed 15 kHz jump in ω, the corresponding 50 fm change in z is however below the resolution of our measurement.
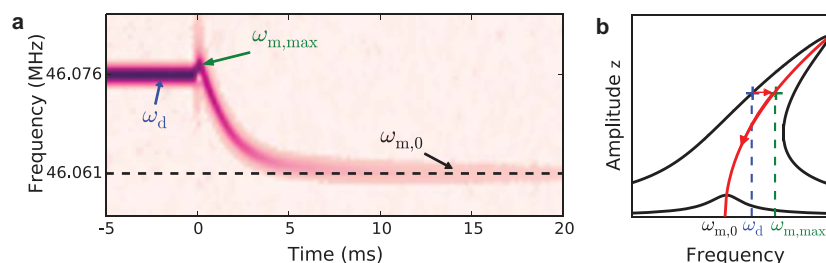
Figure S11: **Short-time Fourier transform of the vibration during the decay.** **a**, Vibration frequency as a function of time during the decay (same data as in the main text). **b**, Schematic showing the relation between the driven spectral response (black) and the free decay (red). The two black curves correspond to the driven spectral response for high and low driving force amplitudes. When the driving force is stopped, the vibration frequency switches from ω_d to $\omega_\mathrm{m,max}$ and then evolves during the decay along the amplitude dependent eigenfrequency towards $\omega_\mathrm{m,0}$.

S.7.2   Energy decay when the frequency ratio of two modes is not strictly an integer

The crossover in the decay rate is also observed in device II when tuning the gate voltage away from the 3:1 internal resonance condition at $V_\mathrm{g} = -3.3$ V. (Figure S12). However, the amplitude where the decay rate changes gets larger (blue curve). This is in agreement with the increased energy that is required to overcome the frequency detuning and induce mode hybridization.

S.7.3   Energy decay measurements compared to the predictions with the dissipative force $F = \eta z^2 \dot{z}$

Previous spectral measurements of nonlinear damping in nanotube and graphene resonators were analysed using a dissipation force $F = \eta z^2 \dot{z}$ with η a constant [7]. Here, we show that this nonlinear damping force cannot account for our energy decay measurements. The equation of motion is

$$\ddot{z}(t) + \omega_1^2 z(t) + \left[\gamma_1 + \frac{\eta}{m_\mathrm{eff}} z^2(t) \right] \dot{z}(t) + \alpha_1 z^3(t) = F_\mathrm{d}(\omega_\mathrm{d})/m_\mathrm{eff} \tag{S5}$$

with α_1 the Duffing nonlinear constant and $F_\mathrm{d}(\omega_\mathrm{d})$ the oscillating force at frequency $\omega_\mathrm{d}/2\pi$ [7, 8]. In the absence of dephasing, the value of α_1 can be obtained from spectral measurements by plotting the shift of the resonant frequency $\Delta\omega_1$ as a function of the largest vibrational amplitude z_max of the driven spectra. From Eq. (S5) this dependence can be approximated by [8]

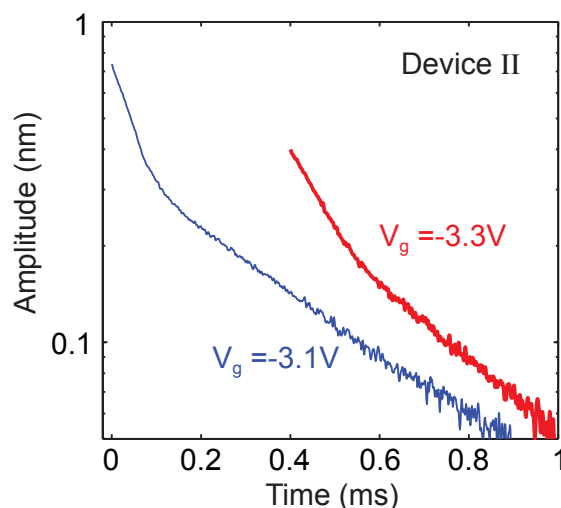$$\Delta\omega_1 = \frac{3}{8}\frac{\alpha_1}{\omega_1} z_\mathrm{max}^2 \tag{S6}$$

Figure S12: **Energy decay away from the exact 3:1 internal resonance condition.** At $V_g = -3.1$ V (blue trace) the change of the dissipation rate occurs at a higher amplitude compared to the energy decay at $V_g = -3.3$ V (red).

where ω_1 is the resonant frequency at low driving force. The nonlinear dissipation constant η can be extracted from spectral measurements as well. For this, we plot z_{max} divided by the amplitude of the driving force F_d as a function of z_{max}. According to Eq. (S5), this dependence scales as

$$\frac{F_d}{z_{max}} = \frac{\eta \cdot \omega_1 z_{max}^2}{4} + \frac{m_{eff}\omega_1^2}{Q_1} \tag{S7}$$

where Q_1 is the quality factor of the resonator. From Eq. (S5) the energy decay can be approximated by [8]

$$z^2(t) = z_0^2 \cdot \frac{\exp\left[-\frac{t-t_0}{\tau}\right]}{1 + \frac{2\eta}{8m_{eff}} \cdot \tau \cdot z_0^2 \cdot \left(1 - \exp\left[-\frac{t-t_0}{\tau}\right]\right)} \tag{S8}$$

with $z_0 = z(t = 0)$ and $\tau = Q_1/\omega_1$.

In the following, we assume that the dissipative force is given by $F = \eta z^2 \dot{z}$, we extract α_1 and η from spectral measurements, and we show that the measured energy decay cannot be described by the energy decay predicted with the dissipative force $F = \eta z^2 \dot{z}$. Figure S13a shows the driven spectra of device II recorded for different force amplitudes F_d. We extract z_{max} and $\Delta\omega_1$ for each spectrum. From the plots of $\Delta\omega_1$ and z_{max}/F_d as a function of z_{max} (Figs. S13b,c), we get that $\alpha_1 = -8.3 \cdot 10^{32}$ m^{-2}s^{-2}, $\eta = 6 \cdot 10^6$ kg/m^{2}s, and $Q_1 = 55\,000$ using Eqs. (S6),(S7). Here we use $m_{eff} = 60$ fg from section S.1. Figure S13d shows that the measurement of the energy decay is not described by Eq. (S8) using the values of α_1, η, and Q_1 determined above. To conclude, this analysis indicates that
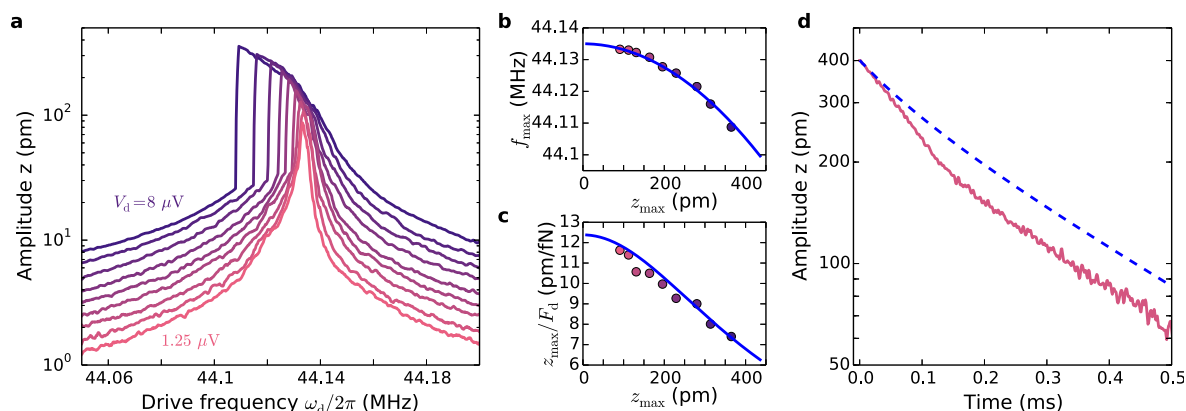
Figure S13: **Spectral measurements compared to energy decay measurements.** **a,** Spectral response of the driven motion for increasing drive voltage V_d with ω_d swept from high to low frequency. The measurement is recorded in device II at intermediate vibration amplitude with $V_g = -3.3$ V. **b,** Plot of f_{max} as a function of z_{max}. From the fit with a nonlinear Duffing restoring force, we extract $\alpha_1 = -8.3 \cdot 10^{32}$ m^{-2}s^{-2} and $\omega_1 = 44.135$ MHz. **c,** Plot of z_{max}/F_d as a function of z_{max}. The data can be fitted with $\eta = 6 \cdot 10^6$ kg/m^{2}s and $Q_1 = 55\,000$. **d,** Comparison between energy decay measurement (red line) and prediction with the dissipative force $F = \eta z^2 \dot{z}$ (blue dashed line).

spectral measurements have to be used with care when quantifying nonlinear dissipation. While spectral measurements can be described with $F = \eta z^2 \dot{z}$ in a satisfactory way, energy decay measurements show a strong deviation from such a dissipation process.

S.8 Theoretical modeling of the 3:1 internal resonance

To model the dynamics which governs the 3:1 internal resonance, $\omega_2 \approx 3\omega_1$, we consider two interacting Duffing oscillators with mode coordinates $q_{1,2}$ coupled via the interaction Hamiltonian $H_{int} = mgq_1^3 q_2$. This is the lowest order interaction term that can yield a 3:1 internal resonance. An important feature of this nonlinear coupling term is that the coupling strength depends on energy in the system. The coupling can therefore initially be strong and then shrink into the weak coupling regime, as energy decays during a ring-down. The generalisation to the n:1 internal resonance is straightforward, and leads to the same results, which will be shown in the last section.

The total Hamiltonian is $H = H_1 + H_2 + H_{int}$, where

$$H_j = m\frac{\dot{q}_j^2}{2} + m\omega_j^2 \frac{q_j^2}{2} + \frac{m}{4}\alpha_j q_j^4, \quad \text{with } j = 1, 2 \tag{S9}$$

$$H_{int} = mgq_1^3 q_2. \tag{S10}$$

The Duffing nonlinearities $\propto \alpha_j q_j^4$ are typically strong in graphene membrane resonators originating from the geometric nonlinearity. In principle it results in nonlinear terms to all orders, but for small amplitudes it usually suffices to keep only the lowest order terms. While we have truncated the expansion at fourth order in oscillator coordinates, we have also omitted non-resonant terms such as $\propto q_1 q_2^3$ and $\propto q_1^2 q_2^2$. These terms are typically dispersive, i.e., introducing additional energy-dependent frequency-shifts, akin to the shifts from the Duffing terms or renormalization of the latter. As we are mainly concerned with capturing the measured behaviors of the system (frequency saturation, plateaus, and kinks in the ring-down traces) with a minimal set of fitting parameters, we limit ourselves to the coupling term $g q_1^3 q_2$. The corresponding equations of motion, introducing drive f and linear dissipation $\gamma_{1,2}$, are

$$\ddot{q}_1 + \gamma_1 \dot{q}_1 + \omega_1^2 q_1 + \alpha_1 q_1^3 + 3 g q_1^2 q_2 = f \cos(\Omega t) \qquad (S11)$$
$$\ddot{q}_2 + \gamma_2 \dot{q}_2 + \omega_2^2 q_2 + \alpha_2 q_2^3 + g q_1^3 = 0. \qquad (S12)$$

The system at hand is weakly damped, and we consider the case when the system is close to the internal resonance $|\omega_2 - 3\omega_1|/\Omega \ll 1$ and the external force drives the fundamental mode $|\Omega - \omega_1|/\Omega \ll 1$. We can then adopt the rotating wave approximation (RWA) by introducing complex amplitudes a_j varying slowly on the time-scale of ω_1^{-1},

$$q_j(t) = a_j(t) e^{i\Omega_j t} + a_j^*(t) e^{-i\Omega_j t}, \qquad (S13)$$
$$\dot{q}_j(t) = i\Omega_j (a_j(t) e^{i\Omega_j t} - a_j^*(t) e^{-i\Omega_j t}), \qquad (S14)$$

where $\Omega_1 = \Omega$ and $\Omega_2 = 3\Omega$. The corresponding dynamical equations in the RWA reads

$$\dot{a}_1 = -i\left([\Omega - \omega_1]a_1 - \frac{3}{2\Omega}\alpha_1 a_1 |a_1|^2 + \frac{3}{2\Omega} g a_1^* a_1^* a_2 \right) - \frac{\gamma_1}{2} a_1 + \frac{f}{4\Omega} \qquad (S15)$$

$$\dot{a}_2 = -i\left([3\Omega - \omega_2]a_2 - \frac{1}{2\Omega}\alpha_2 a_2 |a_2|^2 + \frac{g}{6\Omega} a_1^3 \right) - \frac{\gamma_2}{2} a_2. \qquad (S16)$$

The complex amplitudes a_1 and a_2 describe the amplitude and phase of the periodic oscillation which rotates with frequencies Ω and 3Ω respectively. Hence, the periodic motion which is an orbit in coordinate $\{q_1, \dot{q}_1, q_2, \dot{q}_2\}$-space is described by a single point in the quadrature-space $\{\mathrm{Re}\, a_1, \mathrm{Im}\, a_1, \mathrm{Re}\, a_2, \mathrm{Im}\, a_2\}$.

S.8.1 Bifurcation diagram and amplitude response

Changing the parameters in a nonlinear system can cause it to undergo sudden qualitative changes in dynamics, so called bifurcations. For instance, the number of stationary states may change or oscillatory motion may bifurcate (be initiated) at the boundary between regions. The different dynamical regimes are conveniently charted out by means
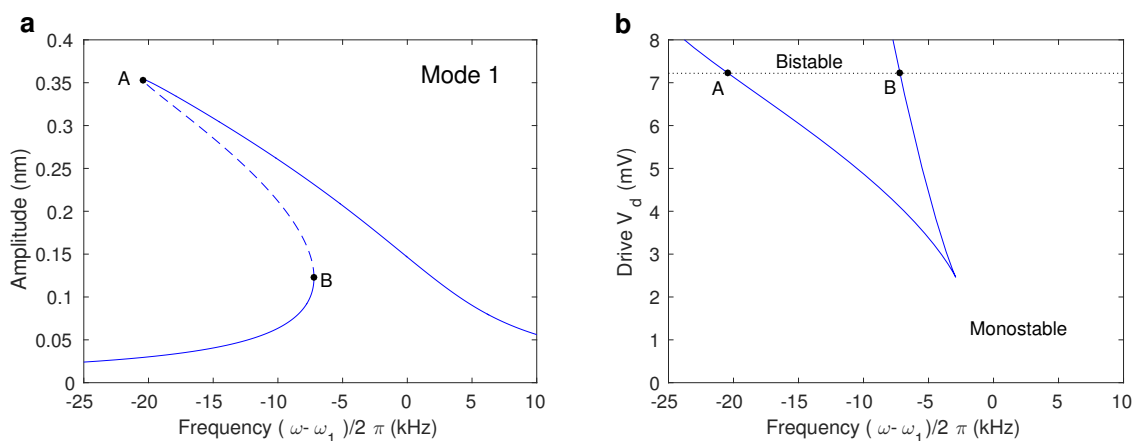
Figure S14: **a**, Amplitude branches of mode one at low drive. The mode basically responds as a driven Duffing oscillator. The system is bistable in the frequency range between bifurcation points A and B. **b**, Corresponding bifurcation diagram. Solid lines separate the monostable and bistable regions. The dashed line corresponds to the amplitude response in the left panel, with bifurcation points A and B indicated.

of bifurcation diagrams, where the locations of the bifurcations are represented by lines separating the qualitatively different regions in parameter space.

To understand the bifurcation diagram connected to the system (S15)-(S16), it is useful to first consider low drive voltages. The system then responds as an independent Duffing oscillator, (see Fig. S14a), containing a region of bistability beween the points A and B. Sweeping the frequency over this region results in hysteresis. For a downward frequency sweep, the system will follow the higher branch until it loses stability at point A, while an upward sweep will switch from the lower branch to the higher branch at point B. Hence, as a consequence of the multi-stability, not all bifurcations crossed in parameter space are observed experimentally during a single frequency sweep. For instance, point B in Fig. S14 is passed unnoticed during the downward frequency sweep, whereas point A is not visible in an upward sweep.

At higher drives the mode coupling becomes stronger, resulting in a more complex bifurcation diagram (see Fig. S15). The solid blue lines correspond to saddle-node (SN) bifurcations where two new states (fix-points) with fixed amplitudes and phases are created. These are easily found by numerically solving for the static solutions to Eqs. (S15)-(S16). The dashed red lines show Hopf (H) bifurcations. At a few points, the Hopf curve undergoes a Bogdanov-Takens bifurcation and continues as a neutral saddle, which is not a bifurcation. Hopf bifurcations involve the change of stability of a fix-point in quadrature space and the emergence of stable or unstable oscillatory motion. Finding Hopf bifurcations is technically more demanding but the Matlab software project `matcont` [20] offers an efficient implementation to find the bifurcations. We will refer to the bifurcations in
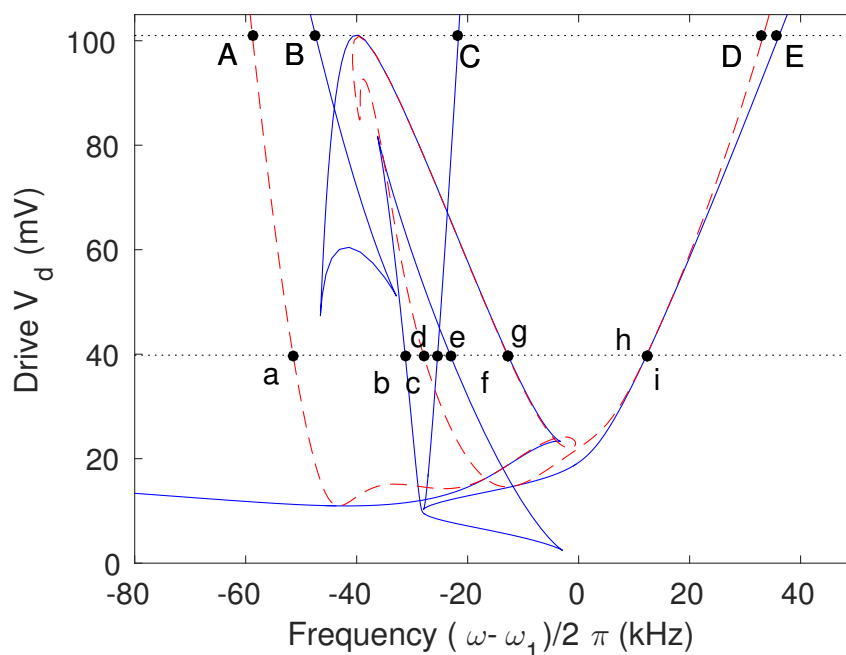
Figure S15: Bifurcation diagram for the system (S15)-(S16) as function of frequency detuning and drive strength. The diagram is drawn using the fitted parameter values in table S2. The lines separate regions with different qualitative dynamical behavior. Blue solid lines correspond to saddle-node bifurcations where two new fixed states appear. The dashed red lines correspond to Hopf bifurcations where the stability of an amplitude branch changes and is accompanied by stable or unstable amplitude modulation of the motion (parts of the lines are neutral saddles). The dashed black lines correspond to frequency sweeps at constant drive voltage (see Figs. S16 and S17), i.e, they are not bifurcation lines.

relation to the rotating frame Eqs. (S15)-(S16). While the bifurcation diagram is identical in the original $\{q_1, \dot{q}_1, q_2, \dot{q}_2\}$-representation, the involved bifurcations are technically different due to the transformation into the rotating wave Eqs. (S13)-(S14).

To relate the bifurcation diagram to the observed frequency response we take as examples two frequency sweeps at fixed drives corresponding to the two horizontal dotted lines in Fig. S15. The changes in amplitude of mode one for these sweeps are shown in Figs. S16 and S17. For strong driving the system crosses three SN bifurcations at the points B, C and E (see Fig. S16). To understand what happens on the Hopf bifurcation, consider the situation when the system is in the stable high-amplitude state in the top left of Fig. S16(a). If the driving frequency is increased, the system follows the stable branch until point A. Here the system undergoes a (supercritical) Hopf bifurcation which changes
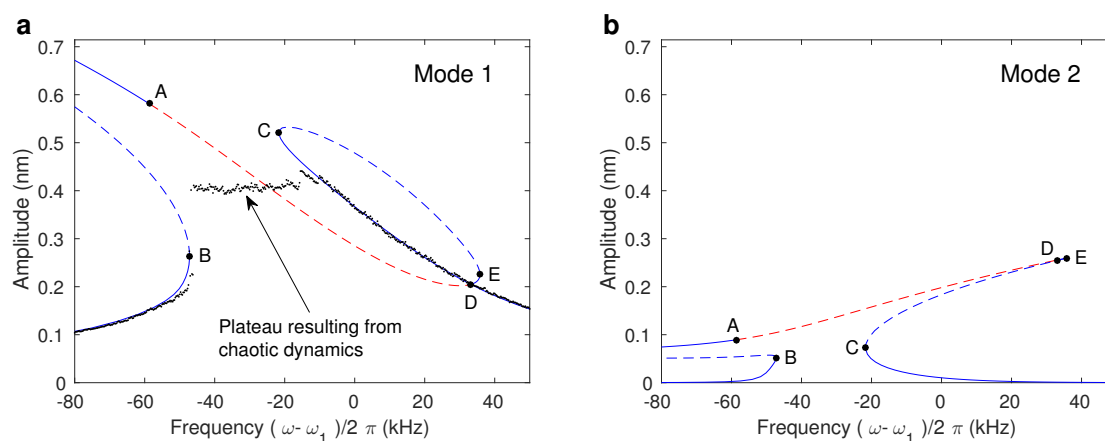
Figure S16: Amplitude branches of mode one (**a**) and two (**b**) corresponding to the upper dashed line frequency sweep in Fig. S15. The bifurcation points A-E correspond to the bifurcations crossed in Fig. S15. Hopf bifurcations take place at point A and D which initiate and terminate an amplitude modulated solution. Note that mode 2 is not discontinuously actuated close to the internal resonance where the plateau of mode one (indicated by the experimental data points) is observed.

the stability of the stationary state to become unstable. At the same time, stable periodic orbits (limit cycles) in the quadrature space bifurcate from the Hopf-point, introducing a new frequency into the dynamics. This means that the system no longer performs motion at stable amplitude but instead the motion is amplitude modulated. The state of the system can then no longer be represented as a point in fig. S16. In $\{q_1, \dot{q}_1, q_2, \dot{q}_2\}$-space, the amplitude modulation of the periodic orbit, also called torus state, corresponds to dynamics on the *shell of a donut*. Note that the introduction of the new frequency generally makes the motion quasi-periodic. The system also exhibits chaotic dynamics, and the bifurcation diagram presented here is not complete. Other bifurcation lines such as period doubling bifurcations are not shown, but have been observed in numerical simulation, along with chaotic trajectories.

The plateau observed in the response of mode one is connected to the initiation of torus dynamics and chaotic dynamics. The data points in (Fig. S16-S17) represent the quantity $A = \sqrt{\text{Re}\{\bar{a}_1\}^2 + \text{Im}\{\bar{a}_1\}^2}$, where the bar denotes time averaged quantity. If the system is in a steady oscillatory state, a_1 is time independent and A gives a measure of the energy (amplitude squared). However, if the system is in a torus or chaotic state a_1 is time dependent, resulting in some of the energy being contained in interference terms which are averaged out in the measurement of A. Hence, not all the energy is captured which results in the observed plateau. Note that for the ring-down experiments, the bandwidth of the measurement is larger than the bandwidth during the frequency sweeps. Hence, in the ring-down experiments also the energy in the interference term is measured.
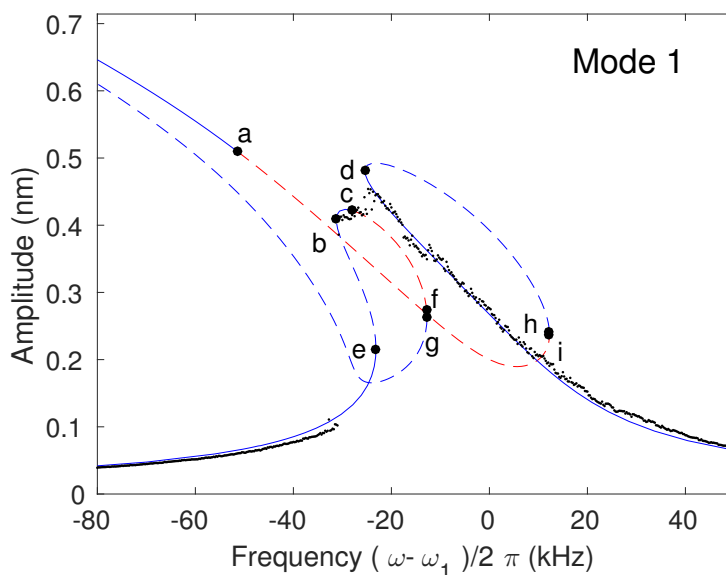
Figure S17: Amplitude branches of mode one corresponding to the lower dashed line frequency sweep in Fig. S15. The bifurcation points a-i correspond to the bifurcations crossed in Fig. S15.

A consequence of the large fluctuations in the chaotic state is that the system hits the SN-point B and drops to the low stable amplitude branch also for downward sweep, (Fig. S16). The strength of fluctuations and basin of attraction for different states determine where the system ends up when there are more than one stable state to switch to (Fig. S17). No stochastic fluctuations were taken into account when simulating the frequency responses.

S.8.2 Determination of the system parameters

The resonance frequency ω_1, the damping rate γ_1 and the Duffing constant α_1 of mode 1 are obtained from the spectral measurements of mode 1 at low drive, as it is usually done with Duffing oscillators. The signal of the spectral measurements of mode 2 is weak, because the resonance frequency ω_2 is much larger than the cavity linewidth. As a result, the resonance of mode 2 can be detected only by applying a large driving force, which drives mode 2 deep into the nonlinear regime. The poor quality of these spectral measurements prevent us from quantifying the damping rate γ_2 and the Duffing constant α_2 of mode 2. Instead, we estimate these parameters as well as the coupling strength g using an iterative process where our model is compared to the measurements of (i) the bifurcations (in Fig. S18a), (ii) the shape of the plateau in the response (Fig. 4b of the
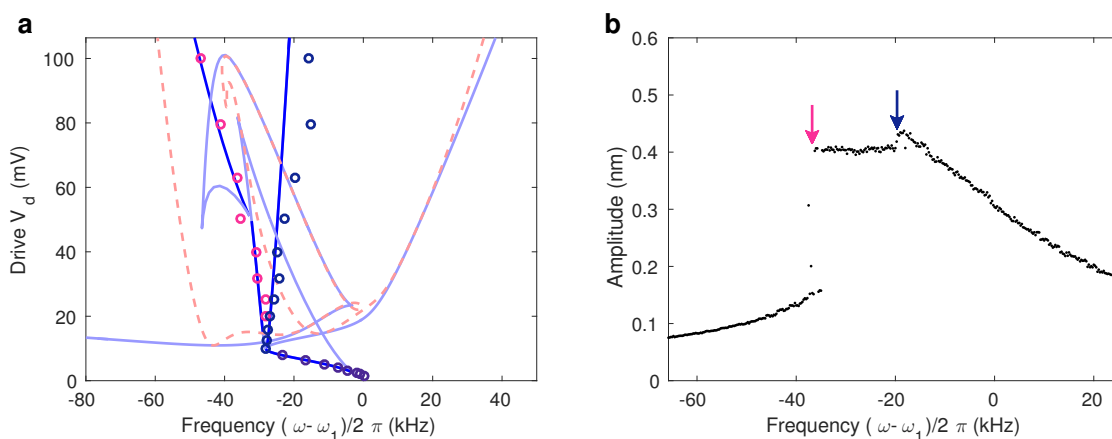
Figure S18: **a**, Experimental data (circles) for the bifurcations in comparison with the theoretically predicted bifurcations. The bifurcation lines that are not observed experimentally are faded. **b**, Measured response. The bifurcation points are experimentally observed as drops in amplitude, see arrows. The data correspond to a downward frequency sweep at $V_d = 63.1$ mV.

main text), (iii) the amplitude response close to the internal resonance (Fig. 4a-b in the main text, as well as Fig. S17) and (iv) the ring-down trace (Fig. 4d of the main text). The resulting parameters are displayed in Table S2. These parameters reproduce the ring-down. The frequency responses are reproduced with identical parameters with the exception of γ_1. As the frequency response is measured using a larger pump power, the damping γ_1 must be increased accordingly (see Fig. S10).

Table S2: System parameters.

Quantity	Value	Quantity	Value
$\omega_1/2\pi$	44.132 MHz	$\gamma_1/2\pi$	993 Hz
$\omega_2/2\pi$	132.25 MHz	$\gamma_2/2\pi$	1.9 kHz
α_1	$-8.3 \cdot 10^{32}$ s^{-2}m^{-2}	g	$1.25 \cdot 10^{33}$ s^{-2}m^{-2}
α_2	$5.25 \cdot 10^{34}$ s^{-2}m^{-2}		

S.8.3   Ring-down with 1:1 internal resonance and linear coupling

In order to understand the energy decay of the coupled system it is instructive to start with a simplified scenario of two linearly coupled and nearly resonant harmonic oscillators.

The equations of motion in RWA are given by

$$\dot{a}_1 = -\frac{i}{2}ga_2 - \frac{\gamma_1}{2}a_1 \tag{S17}$$

$$\dot{a}_2 = -i\left(\delta a_2 + \frac{g}{2}a_1\right) - \frac{\gamma_2}{2}a_2, \tag{S18}$$

where $\delta = \omega_1 - \omega_2$ is the frequency detuning. The system, being linear, has solutions in terms of decaying eigenmodes $u_\pm(t)$ obeying $u_\pm(t) = u_\pm^{(0)}(t)e^{-\lambda_\pm t}$. The eigenvalues $\lambda_\pm$ are given by

$$\lambda_\pm = \frac{1}{2}\left(\frac{\gamma_1 + \gamma_2}{2} + i\delta \pm \sqrt{\left(\frac{\gamma_1 - \gamma_2}{2} - i\delta\right)^2 - g^2}\right) \tag{S19}$$

We can clearly distinguish two cases. Firstly, when $g^2 \gg (\Gamma_-/2)^2 + \delta^2$, $\lambda_\pm \approx \frac{1}{2}(\Gamma_+/2 + i[\delta \pm |g|])$, where $\Gamma_\pm = \gamma_2 \pm \gamma_1$. The system is hybridized and both modes decay with the same rate $\Gamma_+/2$. In the other limit, $g^2 \ll (\Gamma_-/2)^2 + \delta^2$, the two modes are effectively decoupled and ring down with rates $\gamma_1/2$ and $\gamma_2/2$ respectively. Hence, the criterion for observing hybridization during the ring-down is that $g^2 > (\Gamma_-/2)^2 + \delta^2$.

S.8.4 Ring-down with 3:1 internal resonance and nonlinear coupling, energy-phase representation

When the drive is switched off, the reference phase provided by the drive vanishes and the system becomes gauge invariant. This implies that the number of dynamical variables can be reduced from four to three. For the discussion of the transient behavior during the ring-down it is then convenient to work with energy and phase-variables. Defining the variables E_j and ϕ_j such that $a_j = \sqrt{E_j}e^{i\phi_j}/\Omega_j$, (recall that $\Omega_1 = 1$ and $\Omega_2 = 3$) we can formulate the dynamical equations (S15)-(S16) in terms of the mode energies E_1, E_2 and the relative phase $\vartheta = 3\phi_1 - \phi_2$. The corresponding equations for the mode energies and relative phase are

$$\dot{E}_1 = -gE_1\sqrt{E_1E_2}\sin\vartheta - \gamma_1 E_1 \tag{S20}$$

$$\dot{E}_2 = gE_1\sqrt{E_1E_2}\sin\vartheta - \gamma_2 E_2 \tag{S21}$$

$$\dot{\vartheta} = \left[\delta + \frac{9}{2}\alpha_1 E_1 - \frac{1}{18}\alpha_2 E_2\right]$$

$$+ \frac{g}{2}(E_1 - 3E_2)\sqrt{\frac{E_1}{E_2}}\cos\vartheta. \tag{S22}$$

Here, we have introduced the relative mode detuning $\delta = (\omega_2 - 3\omega_1)/\Omega$.

When the modes are strongly hybridized, their mode energies $E_{1,2}$ oscillate around a common mean. It is then convenient to switch to yet another representation where we use

one variable to denote total mode energy and the other variable to represent the relative energy of the two modes. Let E denote the total mode energy, $E(t) = E_1(t) + E_2(t)$. The distribution of energy between the two modes we represent by the variable $\Delta(t) = [E_1(t) - E_2(t)]/[E_1(t) + E_2(t)]$. Changing the time scale to $\tau = gt$ we obtain the dynamical system

$$\dot{E} = -E\Gamma^+ - E\Delta\Gamma^- \tag{S23}$$

$$\dot{\Delta} = -E\frac{1+\Delta}{2}\sqrt{1-\Delta^2}\sin\vartheta - (1-\Delta^2)\Gamma^- \tag{S24}$$

$$\dot{\vartheta} = \delta + E\left(\alpha^- + \Delta\alpha^+ + \left(\Delta - \frac{1}{2}\right)\sqrt{\frac{1+\Delta}{1-\Delta}}\cos\vartheta\right). \tag{S25}$$

Here we have introduced the rescaled dissipation rates $\Gamma^\pm \equiv (\gamma_1 \pm \gamma_2)/g$ and the rescaled detuning $\delta = (3\omega_1 - \omega_2)/g$, and Duffing parameters $\alpha^\pm = (9\alpha_1 \pm \alpha_2/9)/4g$.

At high energies, the hybridized state is characterized by oscillations in Δ corresponding to energy switching back and forth between the two modes. In this regime, we can crudely estimate the time average $\bar{\Delta} \approx 0$ and compare with the weakly damped linearly coupled system. We can then identify the energy dependent detuning $\delta_{\text{eff}} \approx \delta + E\alpha^-$ and the effective energy dependent coupling $g_{\text{eff}} \approx gE$. From the results on the linearly coupled system above (see sec. S.8.3) we thus expect an average exponential like decay with rate of the order of Γ^+ and, the hybridization to be maintained as long as $g_{\text{eff}}^2 > \delta_{eff}^2 + (\Gamma^-/2)^2$, However, as the system energy approaches this value, the above argument breaks down. In particular, we have found that at the energy where the modes decouple, the system may enter a regime of slow dynamics which is not susceptible to this simple estimate. Still, the estimate $g_{\text{eff}}^2 \approx \delta_{eff}^2 + (\Gamma^-/2)^2$ provides a crude upper estimate on the location of the transition.

S.8.5 Ring-down with n:1 internal resonance and nonlinear coupling

In the more general situation of an n:1 internal resonance case, $n > 1$, the frequencies are assumed to be close to the internal resonance $\omega_2 \approx n\omega_1$. The Hamiltonian coupling term (2) is replaces with $gq_1^n q_2$ but still gives very similar physics as the 3:1 internal resonance. The coupling term is energy dependent which allows the system to enter different coupling regions as it rings down.

The equations for the complex amplitudes are in the n:1 case given by

$$\dot{a}_1 = -i\left(\delta_1 a_1 - \frac{3}{2}\alpha_1 a_1 |a_1|^2 + \frac{n}{2}g a_1^{*n-1} a_2\right) - \frac{\gamma_1}{2}a_1 + \frac{f}{2}$$

$$\text{(S26)}$$

$$\dot{a}_2 = -i\left(\delta_2 a_2 - \frac{3}{2n}\alpha_2 a_2 |a_2|^2 + \frac{g}{2n}a_1^n\right) - \frac{\gamma_2}{2}a_2. \quad \text{(S27)}$$

Transforming to energy and phase variables where the energy of the higher mode takes the form $E_2 = n^2|a_2|^2$, the amplitude $a_2 = \sqrt{E_2}\exp(i\phi_v)/n$ and relative phase $\vartheta = n\phi_1 - \phi_2$ result in

$$\dot{E} = -E\Gamma^+ - E\Delta\Gamma^- \quad \text{(S28)}$$

$$\dot{\Delta} = -\left(E\frac{1+\Delta}{2}\right)^{\frac{n-1}{2}}\sqrt{1-\Delta^2}\sin\vartheta - (1-\Delta^2)\Gamma^- \quad \text{(S29)}$$

$$\dot{\vartheta} = \delta + E\left(\alpha^- + \Delta\alpha^+\right) + \left(E\frac{1+\Delta}{2}\right)^{\frac{n-1}{2}}\frac{1-n+\Delta(n+1)}{2\sqrt{1-\Delta^2}}\cos\vartheta.$$

$$\text{(S30)}$$

The energy-dependent coupling becomes stronger with increasing energy to the power $(n-1)/2$ and is constant for $n = 1$. Hence, abrupt variations of the energy decay rates are expected for couplings with $n > 1$ and not just for the $3:1$ internal resonance.

References

[1] Weber, P., Güttinger, J., Tsioutsios, I., Chang, D. E., and Bachtold, A. Coupling graphene mechanical resonators to superconducting microwave cavities. *Nano Letters* **14**(5), 2854–60 (2014).

[2] Eichler, C., Salathe, Y., Mlynek, J., Schmidt, S., and Wallraff, A. Quantum-limited amplification and entanglement in coupled nonlinear resonators. *Phys. Rev. Lett.* **113**, 110502, (2014).

[3] Aspelmeyer, M., Kippenberg, T. J., and Marquardt, F. Cavity optomechanics. *Rev. Mod. Phys.* **86**, 1391–1452, (2014).

[4] Rocheleau, T., Ndukum, T., Macklin, C., Hertzberg, J. B., Clerk, A. A., and Schwab, K. C. Preparation and detection of a mechanical resonator near the ground state of motion. *Nature* **463**(7277), 72–75 (2010).

[5] Ni, Z. H., Wang, H. M., Kasim, J., Fan, H. M., Yu, T., Wu, Y. H., Feng, Y. P., and Shen, Z. X. Graphene thickness determination using reflection and contrast spectroscopy. *Nano Letters* **7**(9), 2758–2763 (2007).

[6] Blake, P., Hill, E. W., Castro Neto, A. H., Novoselov, K. S., Jiang, D., Yang, R., Booth, T. J., and Geim, A. K. Making graphene visible. *Applied Physics Letters* **91**(6), – (2007).

[7] Eichler, A., Moser, J., Chaste, J., Zdrojek, M., Wilson-Rae, I., and Bachtold, A. Nonlinear damping in mechanical resonators made from carbon nanotubes and graphene. *Nature Nanotech.* **6**(6), 339–342 (2011).

[8] Lifshitz, R. and Cross, M. Nonlinear dynamics of nanomechanical and micromechanical resonators. *Reviews of nonlinear dynamics and complexity* **1**, 1–48 (2008).

[9] Nayfeh, A. H. and Mook, D. T. *Nonlinear oscillations.* John Wiley & Sons, (2008).

[10] Antonio, D., Zanette, D. H., and Lopez, D. Frequency stabilization in nonlinear micromechanical oscillators. *Nature Commun.* **3**, 806, (2012).

[11] Song, X., Oksanen, M., Sillanp, M. A., Craighead, H. G., Parpia, J. M., and Hakonen, P. J. Stamp transferred suspended graphene mechanical resonators for radio frequency electrical readout. *Nano Letters* **12**(1), 198–202 (2012).

[12] Lassagne, B., Tarakanov, Y., Kinaret, J., Garcia-Sanchez, D., and Bachtold, A. Coupling mechanics to charge transport in carbon nanotube mechanical resonators. *Science* **325**(5944), 1107–1110 (2009).

[13] Gonnelli, R. S., Paolucci, F., Piatti, E., Sharda, K., Sola, A., Tortello, M., Nair, J. R., Gerbaldi, C., Bruna, M., and Borini, S. Temperature dependence of electric transport in few-layer graphene under large charge doping induced by electrochemical gating. *Scientific Reports* **5**, 9554, (2015).

[14] Chen, C., Rosenblatt, S., Bolotin, K., Kalb, W., Kim, P., Kymissis, I., Stormer, H., Heinz, T., and Hone, J. Performance of monolayer graphene nanomechanical resonators with electrical readout. *Nature Nanotech.* **4**(12), 861–867 (2009).

[15] van der Zande, A. M., Barton, R. A., Alden, J. S., Ruiz-Vargas, C. S., Whitney, W. S., Pham, P. H. Q., Park, J., Parpia, J. M., Craighead, H. G., and McEuen, P. L. Large-scale arrays of single-layer graphene resonators. *Nano Letters* **10**(12), 4869–4873 (2010).

[16] Imboden, M. and Mohanty, P. Dissipation in nanoelectromechanical systems. *Physics Reports* **534**(3), 89 – 146 (2014).

[17] Kleiman, R. N., Agnolet, G., and Bishop, D. J. Two-level systems observed in the mechanical properties of single-crystal silicon at low temperatures. *Phys. Rev. Lett.* **59**, 2079–2082, (1987).

[18] Rivière, R., Deléglise, S., Weis, S., Gavartin, E., Arcizet, O., Schliesser, A., and Kippenberg, T. J. Optomechanical sideband cooling of a micromechanical oscillator close to the quantum ground state. *Phys. Rev. A* **83**, 063835, (2011).

[19] Lulla, K. J., Defoort, M., Blanc, C., Bourgeois, O., and Collin, E. Evidence for the role of normal-state electrons in nanoelectromechanical damping mechanisms at very low temperatures. *Phys. Rev. Lett.* **110**, 177206, (2013).

[20] $MATCONT$, $CL\_MATCONT$ and $CL\_MATCONT\_for\_MAPS$ continuation software in Matlab, version matcont6p2 (2015-05-21), http://www.matcont.ugent.be/